ADVANCED MATERIALS
www.advmat.de

Ultrathin and Conformable Lead Halide Perovskite Photodetector Arrays for Potential Application in Retina-Like Vision Sensing

Wenqiang Wu, Xun Han, Jing Li, Xiandi Wang, Yufei Zhang, Zhihao Huo, Qiushuo Chen, Xidi Sun, Zhangsheng Xu, Yongwen Tan, Caofeng Pan, and Anlian Pan**

Solution-processed lead halide perovskites are considered one of the promising materials for flexible optoelectronics. However, the array integration of ultrathin flexible perovskite photodetectors (PDs) remains a significant challenge limited by the incompatibility of perovskite materials with manufacturing techniques involving polar liquids. Here, an ultrathin (2.4 µm) and conformable perovskite-based PD array (10 × 10 pixels) with ultralight weight (3.12 g m^{-2}) and excellent flexibility, is reported. Patterned all-inorganic $CsPbBr_3$ perovskite films with precise pixel position, controllable morphology, and homogenous dimension, are synthesized by a vacuum-assisted drop-casting patterning process as the active layer. The use of waterproof parylene-C film as substrate and encapsulation layer effectively protects the perovskite films against penetration of polar liquids during the peeling-off process. Benefitting from the encapsulation and ultrathin property, the device exhibits long-term stability in the ambient environment, and robust mechanical stability under bending or 50% compressive strain. More importantly, the ultrathin flexible PD arrays conforming to hemispherical support realize imaging of light distribution, indicating the potential applications in retina-like vision sensing.

Ultrathin flexible optoelectronic devices, employing novel materials (e.g., 2D materials and perovskite materials),[1] are emerging as a candidate in the rapidly advancing fields, such as wearable devices,[2] soft robotics,[3] and healthcare monitoring,[4] due to the lightweight feature, ultra-flexibility, and conformal contact.[5] In particular, perovskite materials with remarkable physical properties,[6] as one of the most promising semiconductor materials, could be synthesized on various substrates with low-cost solution-processed methods at modest synthetic conditions, opening exciting directions for the fabrication of ultrathin flexible optoelectronic devices.[7] For instance, ultrathin and flexible lead halide perovskite solar cells (SCs) with improved durability, conformability as well as signal quality, have been demonstrated and applied on curved surfaces.[8] Likewise, as a vital device for image sensing, photodetector (PD) arrays manufactured into the ultrathin device can reduce their rigidity to prevent degradation of photoelectric performances when mechanical deformation occurs, making it possible to capture images on a 3D curved surface.[9] However, the fabrication of ultrathin flexible perovskite-based PD arrays remains a significant challenge, due to perovskite materials not being compatible with photolithography techniques, and peeling-off methods involving polar liquids.[10]

To realize the array integration of perovskite-based PDs with excellent flexibility and satisfying mechanical conformability, numerous researchers have made great efforts on the controllable synthesis of materials and the design of devices.[11] Currently, perovskite single-crystal nanowires or microplates and polycrystalline films with controlled morphology were synthesized through newly developed technologies (e.g., micropillar-structured template[12] and spin-coating method[13]), and some of them were employed to fabricate PD arrays mainly by using polyethylene terephthalate (PET) as substrate, yielding flexible device with the imaging capability of light distribution.[14] Nevertheless, these PD arrays have limited flexibility, and thus can only work under simple bending deformation, which seriously hinders their practical applications. Besides, an ultrathin multiplexed photodetector based on patterned

W. Wu, Prof. Y. W. Tan, Prof. A. L. Pan
Key Laboratory for Micro-Nano Physics and Technology of Hunan Province
State Key Laboratory of Chemo/Biosensing and Chemometrics
College of Materials Science and Engineering
Hunan University
Changsha 410082, China
E-mail: anlian.pan@hnu.edu.cn

W. Wu, J. Li, Dr. X. Wang, Y. Zhang, Z. Huo, Q. Chen, X. Sun, Z. Xu, Prof. C. F. Pan
CAS Center for Excellence in Nanoscience
Beijing Key Laboratory of Micro-Nano Energy and Sensor
Beijing Institute of Nanoenergy and Nanosystems
Chinese Academy of Sciences
Beijing 100083, P. R. China
E-mail: cfpan@binn.cas.cn

Dr. X. Han
College of Mechatronics and Control Engineering
Shenzhen University
Shenzhen 518060, China

Prof. C. F. Pan
School of Nanoscience and Technology
University of Chinese Academy of Sciences
Beijing 100049, P. R. China

The ORCID identification number(s) for the author(s) of this article can be found under https://doi.org/10.1002/adma.202006006.

DOI: 10.1002/adma.202006006

$CH_3NH_3PbI_3$ film was reported,[15] but this organic–inorganic hybrid perovskite is vulnerable to moisture in the surrounding environment.[16] All-inorganic perovskite materials with uncompromised photoelectronic properties but enhanced environment stability, such as all-inorganic $CsPbBr_3$ perovskite, are potential alternatives in optoelectronic devices.[17] To date, few works on the patterned growth of all-inorganic perovskite films are reported, due to the lack of controlled nucleation and crystallization process.[18] Therefore, it is urgently required to further explore the controllable growth of all-inorganic perovskite materials as well as device fabrication technologies for ultrathin flexible perovskite-based PD arrays.

Here, we introduce an ultrathin (2.4 µm) and conformable perovskite PD array (10 × 10 pixels) by employing stable all-inorganic $CsPbBr_3$ perovskite films as photosensitive material and waterproof parylene-C films as substrate and encapsulation layer for potential applications in artificial vision sensing. To satisfy the demand of PD arrays for independent photosensing units, a vacuum-assisted drop-casting patterning (VADP) process was proposed, achieving the controllable synthesis of the $CsPbBr_3$ film arrays with precise pixel position, controllable morphology, and homogenous dimension. Benefiting from the ultrathin property, the fabricated device with ultralight weight (3.12 g m^{-2}) could be attached to an irregular 3D surface, showing excellent flexibility and conformal contact characteristics. Meanwhile, the device exhibits long-term stability with a slight photocurrent decay of about 5%, ensuring the dynamic photoresponse capability after storing in the ambient environment for 6 weeks and robust mechanical stability with nearly unchanged photosensing ability under bending or 50% compressive strain. More importantly, the ultrathin PD arrays conforming to hemispherical support with homogenous photoresponse from all pixels, can realize imaging of light distribution, indicating the potential applications in artificial vision sensing.

The overall structure of ultrathin flexible PD arrays is schematically displayed in **Figure 1**a. The device is comprised of 10 × 10 individually addressable pixels, which contain five layers of materials with a layer of parylene-C film as the substrate, Au film, SiO_2 film, $CsPbBr_3$ film, and another layer of parylene-C film as the encapsulation layer. Figure 1b shows the cross-sectional schematic of the individual pixel. Transparent 1.1 µm-thick parylene-C film with uniform and dense surface was adopted as the substrate and encapsulation layer, due to its water resistance and excellent flexibility (Figure 1c). The customized circuit, which was made of 50 nm-thick Au film, and a 30 nm-thick SiO_2 film, which served as a hydrophilic/hydrophobic treatment auxiliary layer, were formed on the substrate, respectively. Subsequently, the $CsPbBr_3$ film arrays were neatly arranged on the electrodes, each with dimensions of 100 × 100 µm; the scanning electron microscopy (SEM) image is displayed in Figure 1d. Considering that the increased thickness of perovskite film can enlarge the risk of material destroying under deformation, thin film (≈150 nm-thick) was employed in the device with satisfying film formation quality (Figure 1e). Finally, the entire device was

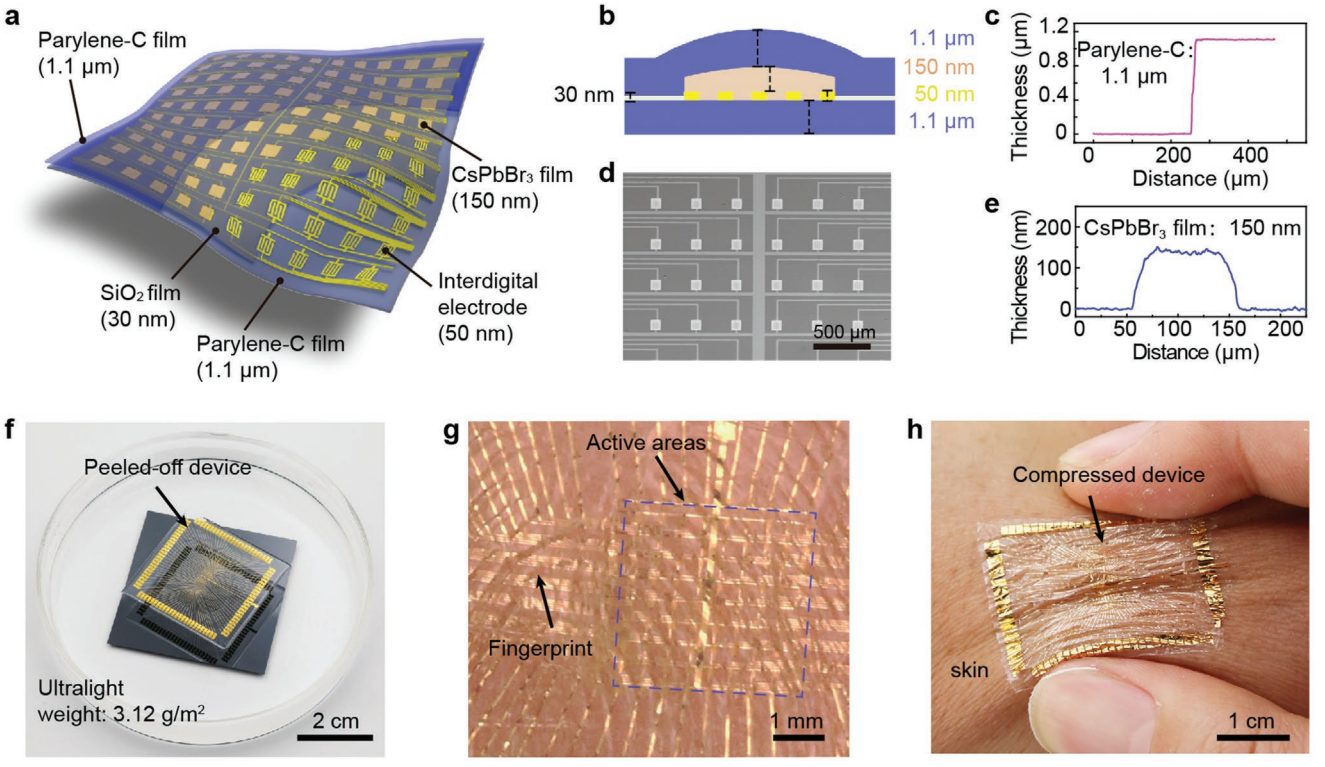

Figure 1. Structural characterization of ultrathin photodetector arrays. a,b) Schematic structure of the ultrathin device and the cross-section of an individual pixel. c) The thickness of the ultrathin parylene-C film. d) SEM image of the active area. e) The thickness of the $CsPbBr_3$ films. f) Photograph of the peeled-off device with ultra-lightweight (3.12 g m^{-2}) floating on the NaCl solution. g) Photograph of the ultrathin device attached on a finger, forming a surface that is consistent with the complex topography of the fingerprint. h) The ultrathin device is laminated on the skin and survives being compressed like the elastomers.

encapsulated by another layer of parylene-C film, which can effectively prevent the destruction of the perovskite films by polar liquids during the peeling-off process. As the thickness of each layer is determined, the total thickness of the ultrathin PD arrays was calculated at about 2.4 μm, to our knowledge, which is the thinnest as well as the most flexible perovskite-based PD arrays (Detailed comparisons are summarized in Table S1, Supporting Information). Besides, the weight of the device is only 3.12 g m^{-2}, which is 25 times lighter than a standard A4 paper (80 g m^{-2}) (Figure S1, Supporting Information).

A crucial step in the device fabrication process is complete exfoliation of the ultrathin device from the p-Si support wafer without wrinkles and damage. In this work, the use of waterproof parylene-C film as the substrate and encapsulation layer solves the incompatibility issue between perovskite materials and peeling-off methods involving polar liquids. Therefore, we employed the electrochemical delamination method as a high-efficiency approach to achieve non-destructive exfoliation within 1 min.[19] This process was conducted in 2 M sodium chloride (NaCl) electrolyte solution with p-Si support wafer connecting to the positive of the power supply (20V) and a Pt flake as the counter electrode. The detailed fabrication process of the device could be found in the Experimental Section and Figures S2 and S3, Supporting Information. As presented in Figure 1f, the ultrathin device was floating on the NaCl solution after being completely exfoliated from the Si wafer, showing the smooth surface without damage. The ultrathin device could be scooped and laminated on the various irregular 3D surface covered by small features, forming intimate contact. Figure 1g shows a photograph of the ultrathin device attached to a finger, demonstrating a curvilinear and uneven surface of the device that is consistent with the complex topography of the fingerprint. The unprecedented mechanical properties of the device are illustrated in Figure 1h and Figure S4, Supporting Information, in which it survives being bent and compressed like the elastomers without delamination from the skin.

Under the requirement of PD arrays for independent photosensing units, we proposed a patterning strategy for all-inorganic $CsPbBr_3$ perovskite film arrays with precise pixel position, controllable morphology, and homogenous dimension. This strategy consists of the patterning of the precursor solution through a pretreated substrate followed by the vacuum-assisted crystallization at room temperature. The drop-casting method was adopted to pattern precursor solution, which allowed sufficient precursor solution remained in the hydrophilic areas, facilitating the formation of compact $CsPbBr_3$ perovskite film. The overall growth process for $CsPbBr_3$ film arrays is schematically shown in **Figure 2**a. Briefly, the precursor solution

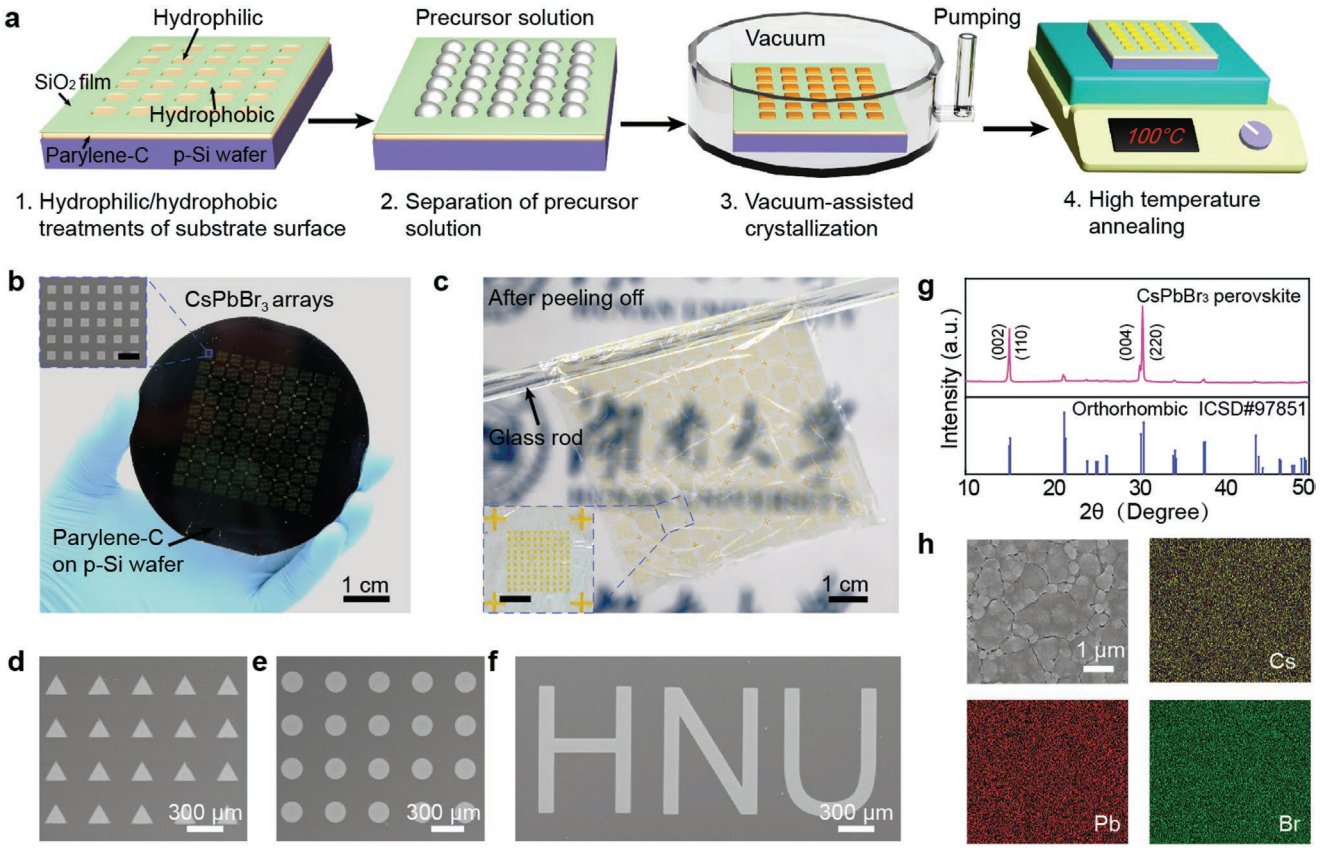

Figure 2. $CsPbBr_3$ arrays synthesis process and characterization. a) Schematic illustration of the $CsPbBr_3$ film arrays synthesis process. b) Photograph of large-scale $CsPbBr_3$ arrays grown on 4-in. p-Si wafer covered with parylene-C film. Inset: the corresponding SEM image. Scale bar: 500 μm. c) Peeled-off $CsPbBr_3$ arrays sandwiched by two ultrathin parylene-C layers. Inset: photograph of magnified $CsPbBr_3$ arrays. Scale bar: 2 mm. d–f) As-grown $CsPbBr_3$ arrays with different geometries, including triangular, circular, and alphabetical patterns. g) X-ray diffraction profile of $CsPbBr_3$ film. h) EDS mapping images of the Cs, Pb, and Br elements distribution.

was first drop-casted onto the pretreated substrate, leading to a homogeneous distribution of liquid domains in the hydrophilic areas (Figures S5 and S6, Supporting Information). Then, the substrate was immediately put into a vacuum drying oven to make it crystallized at room temperature. When the sample was exposed to a low-pressure environment, the evaporation rate of the solvent was accelerated, boosting the rapid crystallization of $CsPbBr_3$ films.[20] With the evaporation of the dimethyl sulfoxide (DMSO), the $CsPbBr_3$ films were crystallized in the hydrophilic areas, realizing patterned growth of compact $CsPbBr_3$ film. To improve the film quality, an annealing process was performed at 100 °C for about 10 min. In the contrast, large crystalline perovskite islands formed when $CsPbBr_3$ perovskite crystallized in the atmospheric environment (Figures S7, Supporting Information). This is because the relatively low solvent evaporation rate allows fewer nucleation sites forming during the crystallization process and facilitates the growth of large crystals, however, sacrificing the coverage rate of a single pixel. The detailed process can be found in the Experimental Section. We envision that a similar fabrication process can apply to other solution-processed semiconductors.

Large-scale $CsPbBr_3$ perovskite film arrays were fabricated through the VADP process on a 4-in. p-Si wafer covered with parylene-C film, as shown in Figure 2b. The SEM image of the perovskite films illustrates neatly arranged film arrays with uniform shape and clear edge (Inset in Figure 2b). Figure 2c demonstrates the photograph of the large-scale $CsPbBr_3$ film arrays after peeling off, sandwiched by two ultrathin parylene-C layers. It is also found that the dimensions of a single pixel are consistent with the corresponding hydrophilic area prepared on the substrate. Thus, various $CsPbBr_3$ arrays with different geometries, including triangular, circular, and alphabetical patterns, are achieved through the VADP process by changing the mask in the photolithography process, as shown in Figure 2d–f and Figure S8, Supporting Information. The $CsPbBr_3$ film arrays with different dimensions were also synthesized, as presented in Figure S9, Supporting Information. Besides, the thickness of as-synthesized $CsPbBr_3$ films is mainly determined by the dimensions of hydrophilic regions and the concentration of the precursor solution. As shown in Figure S10a, Supporting Information, the larger dimensions of the hydrophilic surface gave rise to thicker perovskite films, which is because a hydrophilic surface with larger areas can store more precursor solution. Figure S10b, Supporting Information summarizes the relation between film thickness and precursor concentration at the same dimension of $100 \times 100\ \mu m^2$. The thickness of the as-synthesized films decreases by reducing the concentration of the precursor. Consequently, we believe that this VADP method is versatile with controllable pixel geometry, dimensions, and thickness. Figure 2g shows the X-ray diffraction (XRD) profile; two strong characteristic diffraction peaks were found at 15.2°, 30.7°, which was indexed to (110), (220) orthorhombic crystallographic planes of $CsPbBr_3$ perovskite structure. The clear splitting of the (004) and (220) peaks further indicates that it is consistent with the previously reported room-temperature orthorhombic phase.[21] The elementary composition of our fabricated perovskite film was analyzed by energy-dispersive X-ray spectroscopy (EDS), as shown in Figure 2h, all elements were distributed homogeneously across the whole film. Quantitative analysis was shown in Figure S11, Supporting Information, revealing that the Cs, Pb, and Br elements atomic ratio is 0.88:1:3.06, which is close to the $CsPbBr_3$ ideal stoichiometry.

The photoresponse of an individual pixel was investigated to evaluate the optoelectronic properties of the PD arrays. **Figure 3**a presents the current-voltage (*I–V*) curves of the device in the dark and under 450 nm illumination with different power density. The dark current of the device at 5 V bias voltage was as low as 2×10^{-10} A, while it increased to 5.8×10^{-7} A under the illumination of 10.37 mW cm^{-2}, which exhibits three orders of magnitude higher than the dark current. The current-time (*I–t*) curves of an individual pixel were tested under the illumination of 5.8 mW cm^{-2} (5 V bias) to investigate the dynamic

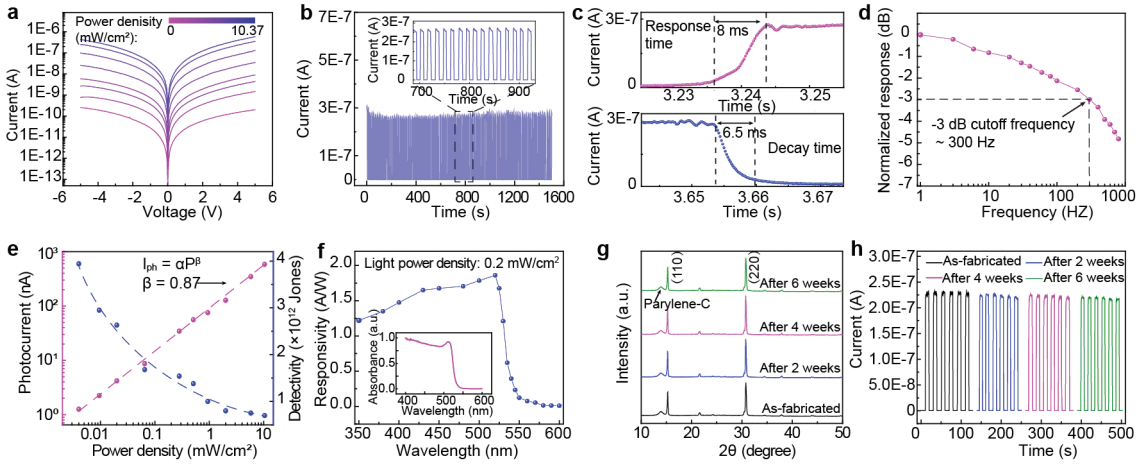

Figure 3. Optoelectronic performances and environmental stability. a) Logarithmic current–voltage (*I–V*) curves of the device measured in the dark and under 450 nm illumination with incident light power density from 0 to 10.37 mW cm^{-2}. b) Current-time (*I–t*) curves of the device under bias voltage of 5 V and the illumination of 5.8 mW cm^{-2}. c) The response time and decay time of the device. d) Normalized photoresponse versus the input signal frequency. e) The dependence of the photocurrent and detectivity on illumination power density. f) The responsivity of device under different wavelengths. The inset is the corresponding absorption spectrum of $CsPbBr_3$ film. g) XRD diffraction peaks of the $CsPbBr_3$ film arrays sandwiched by parylene-C films within 6 weeks. h) Current-time (*I–t*) curves of the device within 6 weeks (Bias voltage of 5 V and illumination power density of 5.8 mW cm^{-2}).

photoresponse (Figure 3b). It can be seen that the performance of the device remained nearly unchanged after operating 1500s (about 100 cycles), indicating the device's stable and reversible photoswitching characteristic. The response speed of the photodetector was further investigated under a pulsed light with different frequencies. Figure S12, Supporting Information, shows the stable temporal response to the pulsed signal with frequencies ranging from 1 to 800 Hz. The response time and decay time of the device measured at 1Hz are about 8 and 6.5 ms, respectively, which are much faster than the response and recovery speed of the human eye (Figure 3c).[22] As shown in Figure 3d, the −3 dB cutoff frequency (f_{-3dB}) of the device was calculated to be ≈300 Hz. The dependence of the photocurrent (I_{ph}) on illumination power density was plotted in Figure 3e (Pink dashed line); it can be fitted by the following equation:

$$I_{ph} = \alpha P^{\beta} \tag{1}$$

where I_{ph} is photocurrent ($I_{ph} = I_{light} - I_{dark}$), P is illumination intensity, α is a constant, β is an exponent related to the photoresponse corresponding to the illumination power density. The best-fitting value of β is 0.87, exhibiting a sublinear power-law behavior. Besides, the specific detectivity (D^*), as a key figure-of-merit of PD, was calculated and presented in Figure 3e (Blue dashed line). Assuming that the total noise limiting the detectivity is major contributed by shot noise from the dark current, it could be calculated by the following equation:[23]

$$D^* = \frac{RA^{1/2}}{(2qI_{dark})^{1/2}} \tag{2}$$

$$R = \frac{I_{ph}}{PA} \tag{3}$$

where R, I_{dark}, P, q, and A are responsivity, dark current, incident light power density, elementary charge, and the effective area of an individual pixel, respectively. The detectivity decreases as illumination intensity increases and it could reach as high as 3.94×10^{12} Jones at an illumination intensity of 4 μW cm^{-2} (R = 3.15 A W^{-1}). Figure 3f depicts the spectral responsivity of the device, showing a broad photoresponse range from 350 to 530 nm, which is consistent with the absorption spectral range of the $CsPbBr_3$ perovskite films. In addition, the dependence of device performances on film thickness was investigated, as shown in Figure S13, Supporting Information. The responsivity increases with the increase of the average film thickness because the thick film can generate more photo-generated carriers under illumination. The response time and decay time decreases nonlinearly as the average thickness increases and tends to be stable when the average thickness increases to 150 nm. Thus, a 150 nm-thick perovskite film was employed for the ultrathin device, considering the optoelectronic and mechanical performances.

The poor tolerance of the perovskite materials to moisture has greatly hindered its practical applications. Especially for polycrystalline perovskite films, water molecules surrounding the atmosphere can easily penetrate into the perovskite material and diffuse due to the inevitable existence of many grain boundaries and pinholes, eventually causing degradation in optical and electrical properties. In this work, the introduction of the waterproof parylene-C film as an encapsulation layer not only prevents the destruction of the perovskite films by polar liquids during the peeling-off process but also blocks the penetration of water molecules in the surrounding environment into perovskite films. As shown in Figure 3g, the as-synthesized $CsPbBr_3$ perovskite films, sandwiched by two ultrathin parylene-C layers, were placed in the ambient environment to investigate the structural stability by monitoring the XRD peaks. All XRD peaks remain unchanged and no new peaks appeared within 6 weeks, proving the long-time structural stability of encapsulated $CsPbBr_3$ perovskite films. In addition, the working stability of the fabricated device in the ambient environment was investigated. As recorded in Figure 3h, the device experienced a slight photocurrent decay of about 5%, ensuring its dynamic photoresponse ability after 6 weeks, which indicates our fabricated ultrathin PD arrays with outstanding environmental stability.

The mechanical robustness of the ultrathin flexible device was characterized under compressive and bending states. As shown in **Figure 4**a, we first laminated the ultrathin device on a pre-stretched elastomer, then carefully released them to introduce a compressive stain inside the device along the direction of pre-stretching. The measurement setups could be found in Figure S14, Supporting Information. Due to the asymmetric structure of the device, irregular wrinkles were formed by the compressive strain. Figure 4b presents the cross-sectional SEM image of the device at 50% compression, showing an extreme mechanical deformation. And wrinkles with a bending radius of fewer than 20 μm have appeared in the folded networks. Despite being subjected to the exfoliation process and extreme compression deformation, the performances of the device are virtually no degradation. As presented in Figure 4c, there is no significant change in output currents of 20 pixels before and after peeling off, which indicates that there is no adverse effect on the device performances during the peeling-off process. The output currents of the device in different compressive strain states were measured, as shown in Figure 4d. No irreversible output current degradation in both dark and illumination conditions was observed until the compressive strain increased to 50%. Figure 4e depicts the corresponding time-dependent photoresponse of the device under 30% and 50% compressive strains. The device shows stable on/off photoswitching behavior, indicating that the ultrathin device can work normally with extreme deformation. To further verify the mechanical durability of the device, the fatigue test of the device at a 50% compressive strain was performed. This test was conducted at a low speed of 0.5 cm s^{-1} to avoid abrupt damage caused by high stretching and releasing speed. As shown in Figure S15, Supporting Information, the photocurrent experienced approximately a 30% decay after 200 compressing cycles while the dark current presented a slight fluctuation, which may attribute to the new wrinkles generated across the perovskite film or the contact change between the electrodes and the perovskite films. In addition, the ultrathin device demonstrates superior mechanical robustness at bending states. As shown in Figure S16, Supporting Information, the dark current and photocurrent were well preserved after 5000 bending cycles and the device exhibited stable photoswitching characteristics. The above investigation results exemplify the excellent mechanical stability of the ultrathin device under the mechanical deformation of bending and compression.

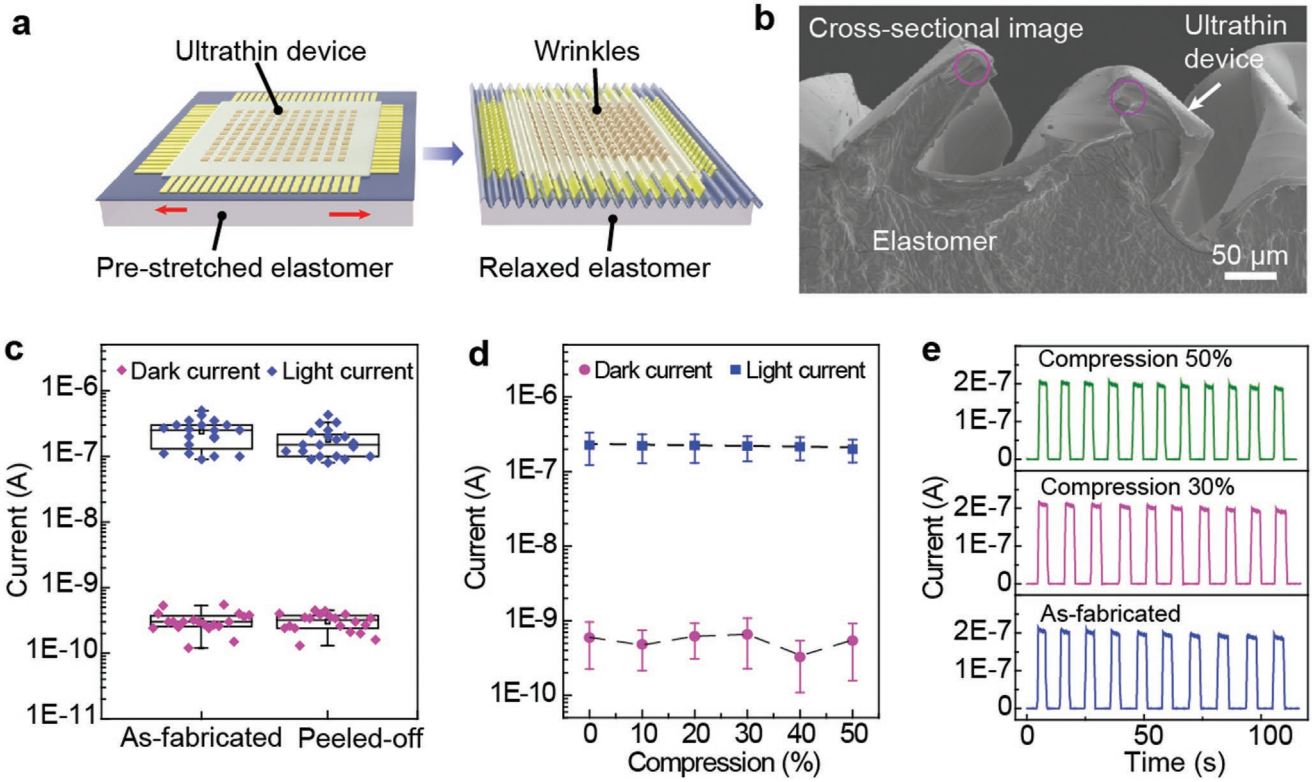

Figure 4. Characterization of mechanical stability of the ultrathin device. a) Schematic illustration of the ultrathin PD arrays undergoing compressive strain. b) Cross-sectional SEM image of the device under 50% compressive strain. c) Output current statistics of 20 pixels in device before and after peeling off. d) The dependence of output current on the different compressive strains. e) Current-time (*I*–*t*) curve of the device without compressed and under different compressive strains (Bias voltage of 5 V and illumination power density of 5.8 mW cm^{-2}).

To further understand the mechanical stability of the ultrathin device under compressive deformation, the strain-stress behavior of the devices with different substrate thicknesses was simulated via the finite element analysis (FEA) method. The model consists of an encapsulation layer of thickness $t_{encapsulation}$, a perovskite layer of thickness $t_{perovskite}$, and a substrate layer of thickness $t_{substrate}$. The thickness of the substrate exhibits a crucial influence on the suffered stress of the perovskite films when the device was compressed. Figure S17, Supporting Information shows the simulation results of the device with $t_{encapsulation}$ of 1 μm, $t_{perovskite}$ of 150 nm, and $t_{substrate}$ ranging from 1 to 25 μm at compression state. When the whole device was compressed, the pixels (perovskite films) distributed at the peaks and valleys of the fold networks were subjected to greater stress compared with other pixels. With the thickness of the substrate decreasing to 1μm, (Figure S17, Supporting Information), the suffered stress of all pixels was reduced, lowering the possibility of damaging pixels. In other words, the device with an ultrathin substrate can effectively withstand higher compressive deformation than the thick devices.

The artificial retina, which mimics the biological functions of human eyes, relies on large-scale PD arrays to realize the recognition function of perceiving images (**Figure 5**a). The ultrathin device with excellent mechanical robustness, which can form conformal contact on irregular surfaces, demonstrates potential application in artificial vision sensing. As shown in Figure 5b,c, our fabricated ultrathin PD arrays were conformed to a walnut, similar to an eyeball. We first verified the uniformity of all pixels by making statistics on the output current. A mercury lamp that can emit white light was employed as a light source for obtaining a large light spot with uniform light power density distribution. As summarized in Figure 5d, the statistical results of dark current reveal that 90% value falls in the interval of 0.33 ± 0.19 nA. Besides, Figure 5e depicts the photocurrent statistics of 10 pixels (a single row) under the homogenous illumination. The photocurrents of these pixels for each illumination intensity are distributed in a narrow range. All the above results indicate that the investigated pixels are functional with satisfactory uniformity. Subsequently, to demonstrate the imaging capability of the device as an artificial retina, the ultrathin device was laminated on hemispherical support and patterned illumination was applied to the active area by using the designed shadow mask, as demonstrated in Figure S18a, Supporting Information. The current of each pixel was collected through the testing pixel by pixel (Figure S18b, Supporting Information). The pixels under illumination (2.5 mW cm^{-2}) can present a higher current, while the other pixels, which are blocked by the shadow mask, have a relatively low current level. As shown in Figure 5f–h, clear letters of "H," "N," and "U" can be identified from the mapping results, which indicates reliable imaging capability of the ultrathin PD arrays on the curved surface.

In summary, we have demonstrated an ultrathin (2.4 μm) and conformable $CsPbBr_3$ perovskite-based PD array with ultralight weight (3.12 g m^{-2}) and excellent flexibility. All-inorganic

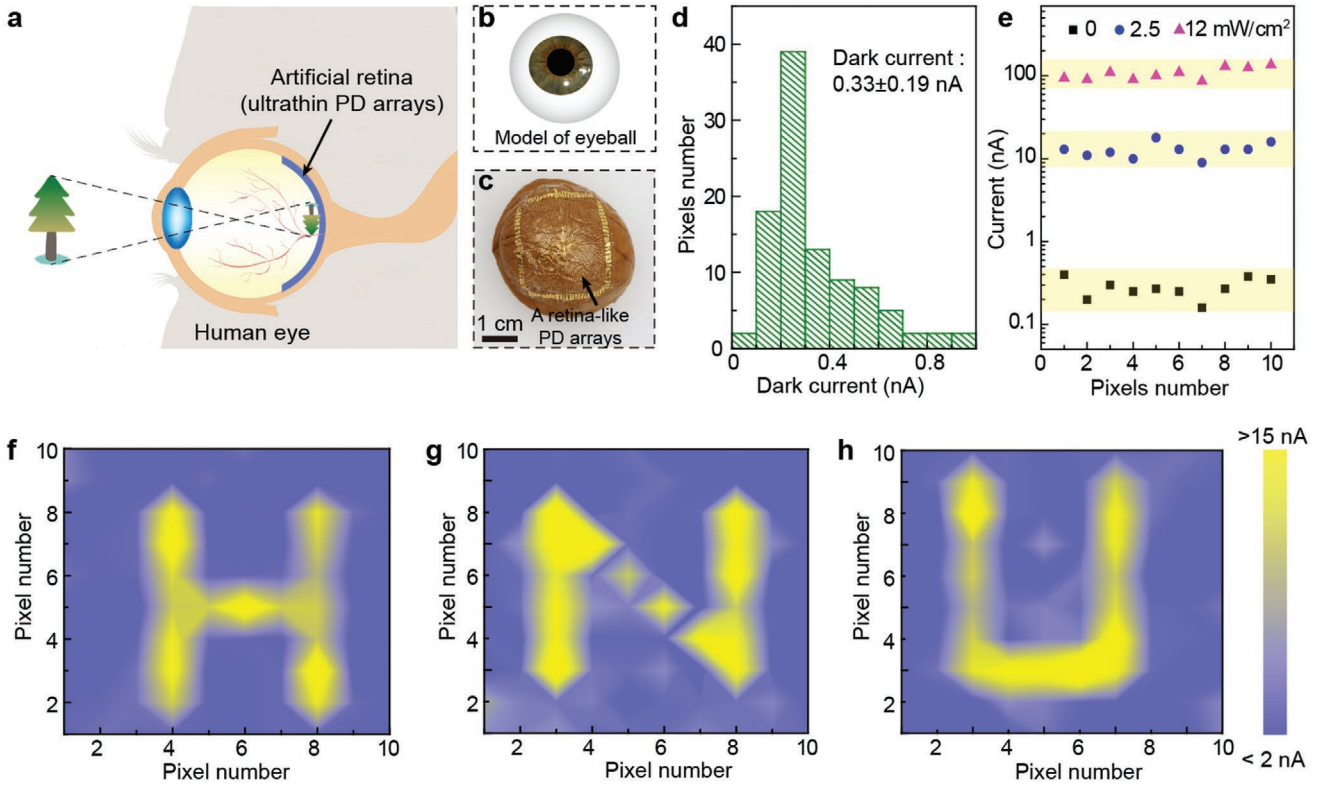

Figure 5. Demonstration of the ultrathin PD arrays imaging capacity. a) A schematic illustration of the ultrathin device with excellent mechanical robustness could be used for artificial vision sensing. b) Model of the eyeball. c) Photograph of ultrathin PD arrays conformed to a walnut. d) The dark current statistics of all pixels under 5 V bias voltage. e) Photocurrent of 10 pixels (a single line) under different illumination. f–h) Light intensity distribution imaging results by the PD arrays laminated on hemispherical support with H-shaped, N-shaped, and U-shaped masks.

$CsPbBr_3$ film arrays with precise pixel position, controllable morphology, and homogenous dimension were synthesized by the VADP process as photosensitive material. We envision that similar fabrication process can be applied to other solution-processed semiconductors. The waterproof parylene-C film was employed as substrate and encapsulation layer, solving the incompatibility issue between perovskite material and manufacturing techniques involving polar liquids. The optoelectronic properties of the as-fabricated device were systematically investigated, showing long-term stability with a slight photocurrent decay of about 5%, ensuring the dynamic photoresponse capability, after storing in the ambient environment for 6 weeks. Besides, owing to ultrathin property, the device remains normally operational when it experiences bending or 50% compressive strain, presenting outstanding mechanical stability. Furthermore, the ultrathin PD arrays conforming to hemispherical support with homogenous photoresponse from all pixels can realize imaging of light distribution, indicating the potential applications in artificial vision sensing.

Experimental Section

Surface Treatments of the Substrate: First, the whole surface of the substrate was treated to be hydrophilic by using oxygen plasma for 60s (power 50 W, O_2 0.2 Torr). Next, the photoresist mask with designed patterns was fabricated by ultraviolet photolithography. Then, SiO_2 film was deposited through radio frequency magnetron sputtering (PVD75 Kurt J. Lesker) as an assisted layer for surface hydrophobic treatment. Sequentially, it was soaked with the solutions of (octadecyl) trichlorosilane (OTS) and hexane at a volume mixing ratio of 1:200 to make the whole surface hydrophobic. After 15 min, the substrate was put into an acetone solution to remove the photoresist and the regions with hydrophilic surfaces covered by photoresist were exposed. After the above treatments, the substrate surface showed hydrophilicity in defined regions and hydrophobicity in other regions.

Controllable Synthesis of the $CsPbBr_3$ Film: Lead bromide ($PbBr_2$) and Cesium bromide (CsBr) at 1:1 mole ratio were mixed in DMSO with different concentration as the precursor solution. The patterned $CsPbBr_3$ film was synthesized by a vacuum-assisted drop-casting patterning process. Specific steps were as follows: First, the precursor solution was drop-casted onto the pretreated substrate, leading to a homogeneous distribution of liquid domains in the hydrophilic area. Second, the substrate was immediately put into a vacuum drying oven to make it rapid crystallized at room temperature. Accompanying the evaporation of the DMSO, $CsPbBr_3$ perovskite tends to crystallize, forming a thin film in the hydrophilic regions. To improve the film quality, an annealing process was performed at 100 °C for about 10 min.

Fabrication of Ultrathin Flexible PD Arrays: For the preparation of an ultrathin flexible substrate, the ultrathin parylene-C film (1.1 µm-thick) was employed and deposited on a p-Si wafer through a polymer organic vapor deposition system (LH 300, LA CHI ENTERPISE CO,. LTD). During the deposition process, the entire system was under vacuum (<30 mtorr) and samples were kept rotating at the speed of 10 rpm min^{-1}. The poly-para-xylylene powders as raw material were first evaporated at 170 °C and cracked to monomers at 650 °C, and then entered into the sample

chamber. The monomer vapor was polymerized to create even parylene-C film on the surfaces of the p-Si wafer in the room temperature chamber. 2 gram of poly-para-xylylene powders could produce a 1.1 µm-thick thin film. Next, designed circuit configuration was fabricated by using ultraviolet photolithography (MA6 SUSS), magnetron sputtering deposition, and conventional lift-off process. Then it was treated as described by surface hydrophilic/hydrophobic treatment method to make the interdigital electrode regions surface hydrophilic and other regions surface hydrophobic. After finishing treatments, the $CsPbBr_3$ film was grown at interdigital electrode regions by vacuum-assisted drop-casting patterning process. Finally, the device was encapsulated by another layer of parylene-C films (1.1 µm-thick). During the deposition process of parylene-C films, all electrode pads were covered through a mask (Teflon tape). When the mask was removed, the electrode pads were exposed for convenience of measurements. After fabricating, an electrochemical delamination method was employed to peel off ultrathin PD arrays from the rigid Si wafer support. It was conducted in 2 M NaCl electrolyte solution; Si wafer was connected to the positive of the power supply (20V), and the Pt flake was used as the counter electrode.

Characterizations and Measurements: The field-emission scanning electron microscopy (SEM) equipped with an energy-dispersive X-ray analyzer (SU8020 Hitachi) and X-ray diffractometer (XRD) were employed to characterize the morphologies, elementary composition, and structure of as-fabricated $CsPbBr_3$ perovskite film. The absorption spectra of the $CsPbBr_3$ perovskite film were investigated by a UV–vis–NIR spectrophotometer (UV-3600 SHIMADZU). The thickness of device was measured by Step Profiler (KLA Tencor P-7 Profiler). Electrical tests were performed by Keithley 4200 SCS, SR570 (Stanford Research Systems), and a probe station (Semiprobe M-6). A laser with tunable wavelength and a high-power mercury lamp (Lumen Dynamics XI120-Q) were used as the illumination source for evaluating the optoelectronic performances and imaging capabilities of the device, respectively. An optical filter was employed to adjust the illumination intensities. A stepping motor (LinMot E1100) was carried out to measure the mechanical stability of the device.

Supporting Information

Supporting Information is available from the Wiley Online Library or from the author.

Acknowledgements

W.W., X.H., and J.L. contributed equally to this work. The authors express thanks for the support of National Natural Science Foundation of China (Nos. U19A2090, 51525202, 51772084, 51972105, 51622205, 61675027), National Key R & D project from Minister of Science and Technology, China (2016YFA0202703), Beijing City Committee of science and technology (Z171100002017019 and Z181100004418004), Natural Science Foundation of Beijing Municipality (2184131, 4181004, 4182080, 4184110, and Z180011), and the University of Chinese Academy of Sciences.

Conflict of Interest

The authors declare no conflict of interest.

Keywords

all-inorganic $CsPbBr_3$ perovskite, artificial vision sensing, conformable contact, photodetector arrays, ultrathin photodetectors

Received: September 2, 2020
Revised: November 19, 2020
Published online: January 21, 2021

[1] a) P. Lin, C. Pan, Z. L. Wang, *Mater. Today Nano* **2018**, *4*, 17; b) J. Sun, Q. Hua, R. Zhou, D. Li, W. Guo, X. Li, G. Hu, C. Shan, Q. Meng, L. Dong, C. Pan, Z. L. Wang, *ACS Nano* **2019**, *13*, 4507.

[2] a) C. Wang, C. Pan, Z. Wang, *ACS Nano* **2019**, *13*, 12287; b) H. Liu, Q. Li, Y. Bu, N. Zhang, C. Wang, C. Pan, L. Mi, Z. Guo, C. Liu, C. Shen, *Nano Energy* **2019**, *66*, 104143; c) H. Jinno, K. Fukuda, X. Xu, S. Park, Y. Suzuki, M. Koizumi, T. Yokota, I. Osaka, K. Takimiya, T. Someya, *Nat. Energy* **2017**, *2*, 780.

[3] a) X. Wang, H. Zhang, R. Yu, L. Dong, D. Peng, A. Zhang, Y. Zhang, H. Liu, C. Pan, Z. L. Wang, *Adv. Mater.* **2015**, *27*, 1405826; b) K. Zhou, Y. Zhao, X. Sun, Z. Yuan, G. Zheng, K. Dai, L. Mi, C. Pan, C. Liu, C. Shen, *Nano Energy* **2020**, *70*, 104546.

[4] Y. J. Hong, H. Jeong, K. W. Cho, N. Lu, D. H. Kim, *Adv. Funct. Mater.* **2019**, *29*, 1808247.

[5] a) S. Wang, J. Xu, W. Wang, G.-J. N. Wang, R. Rastak, F. Molina-Lopez, J. W. Chung, S. Niu, V. R. Feig, J. Lopez, T. Lei, S.-K. Kwon, Y. Kim, A. M. Foudeh, A. Ehrlich, A. Gasperini, Y. Yun, B. Murmann, J. B. H. Tok, Z. Bao, *Nature* **2018**, *555*, 83; b) Y. Li, L. Meng, Y. M. Yang, G. Xu, Z. Hong, Q. Chen, J. You, G. Li, Y. Yang, Y. Li, *Nat. Commun.* **2016**, *7*, 10214; c) J. Kim, H. J. Shim, J. Yang, M. K. Choi, D. C. Kim, J. Kim, T. Hyeon, D. H. Kim, *Adv. Mater.* **2017**, *29*, 1700217; d) X. Wang, Y. Zhang, X. Zhang, Z. Huo, X. Li, M. Que, Z. Peng, H. Wang, C. Pan, *Adv. Mater.* **2018**, *30*, 1706738.

[6] Y. Jiang, X. Wang, A. Pan, *Adv. Mater.* **2019**, *31*, 1806671.

[7] a) W. Deng, H. Huang, H. Jin, W. Li, X. Chu, D. Xiong, W. Yan, F. Chun, M. Xie, C. Luo, L. Jin, C. Liu, H. Zhang, W. Deng, W. Yang, *Adv. Opt. Mater.* **2019**, *7*, 1801521; b) X. Hu, X. Zhang, L. Liang, J. Bao, S. Li, W. Yang, Y. Xie, *Adv. Funct. Mater.* **2014**, *24*, 7373; c) H. Sun, T. Lei, W. Tian, F. Cao, J. Xiong, L. Li, *Small* **2017**, *13*, 1701042; d) H. Sun, W. Tian, F. Cao, J. Xiong, L. Li, *Adv. Mater.* **2018**, *30*, 1706986; e) S. Huang, G. Tang, H. Huang, X.-g. Wu, P. Zhou, L. Zou, L. Xie, J. Deng, X. Wang, H. Zhong, J. Hong, *Sci. Bull.* **2018**, *63*, 1254.

[8] a) M. Kaltenbrunner, G. Adam, E. D. Glowacki, M. Drack, R. Schwodiauer, L. Leonat, D. H. Apaydin, H. Groiss, M. C. Scharber, M. S. White, N. S. Sariciftci, S. Bauer, *Nat. Mater.* **2015**, *14*, 1032; b) M. Kaltenbrunner, M. S. White, E. D. Glowacki, T. Sekitani, T. Someya, N. S. Sariciftci, S. Bauer, *Nat. Commun.* **2012**, *3*, 770.

[9] a) P. Kang, M. C. Wang, P. M. Knapp, S. Nam, *Adv. Mater.* **2016**, *28*, 4639; b) C. Choi, M. K. Choi, S. Liu, M. S. Kim, O. K. Park, C. Im, J. Kim, X. Qin, G. J. Lee, K. W. Cho, M. Kim, E. Joh, J. Lee, D. Son, S. H. Kwon, N. L. Jeon, Y. M. Song, N. Lu, D. H. Kim, *Nat. Commun.* **2017**, *8*, 1664; c) W. Lee, Y. Liu, Y. Lee, B. K. Sharma, S. M. Shinde, S. D. Kim, K. Nan, Z. Yan, M. Han, Y. Huang, Y. Zhang, J. H. Ahn, J. A. Rogers, *Nat. Commun.* **2018**, *9*, 1417; d) H. Schmidt, F. Heuer, H.-J. Wilke, *J. Biomech.* **2009**, *42*, 48; e) X. Han, W. Du, R. Yu, C. Pan, Z. L. Wang, *Adv. Mater.* **2015**, *27*, 1502579.

[10] a) T. Leijtens, K. A. Bush, R. Prasanna, M. D. McGehee, *Nat. Energy* **2018**, *3*, 828; b) H. Wang, D. H. Kim, *Chem. Soc. Rev.* **2017**, *46*, 5204; c) C. Cheng, C. Zhu, B. Huang, H. Zhang, H. Zhang, R. Chen, W. Pei, Q. Chen, H. Chen, *Adv. Mater. Technol.* **2019**, *4*, 1800729.

[11] a) X. Yang, J. Wu, T. Liu, R. Zhu, *Small Methods* **2018**, *2*, 1800110; b) L. Gu, M. M. Tavakoli, D. Zhang, Q. Zhang, A. Waleed, Y. Xiao, K.-H. Tsui, Y. Lin, L. Liao, J. Wang, Z. Fan, *Adv. Mater.* **2016**, *28*, 9713; c) X. Zhang, S. Chen, X. Wang, A. Pan, *Small Methods* **2019**, *3*, 1800294.

[12] J. Feng, X. Yan, Y. Liu, H. Gao, Y. Wu, B. Su, L. Jiang, *Adv. Mater.* **2017**, *29*, 1695003.

[13] J. Wu, J. Chen, Y. Zhang, Z. Xu, L. Zhao, T. Liu, D. Luo, W. Yang, K. Chen, Q. Hu, F. Ye, P. Wu, R. Zhu, Q. Gong, *Nano Lett.* **2017**, *17*, 3563.

[14] a) H. Deng, X. Yang, D. Dong, B. Li, D. Yang, S. Yuan, K. Qiao, Y. B. Cheng, J. Tang, H. Song, *Nano Lett.* **2015**, *15*, 7963; b) W. Deng, X. Zhang, L. Huang, X. Xu, L. Wang, J. Wang, Q. Shang, S. T. Lee,

J. Jie, *Adv. Mater.* **2016**, *28*, 2201; c) W. Wu, X. Wang, X. Han, Z. Yang, G. Gao, Y. Zhang, J. Hu, Y. Tan, A. Pan, C. Pan, *Adv. Mater.* **2018**, *31*, 1805913; d) K. Xia, W. Wu, M. Zhu, X. Shen, Z. Yin, H. Wang, S. Li, M. Zhang, H. Wang, H. Lu, A. Pan, C. Pan, Y. Zhang, *Sci. Bull.* **2020**, *65*, 343; e) W. Hu, W. Huang, S. Yang, X. Wang, Z. Jiang, X. Zhu, H. Zhou, H. Liu, Q. Zhang, X. Zhuang, J. Yang, D. H. Kim, A. Pan, *Adv. Mater.* **2017**, *29*, 1703256.

[15] W. Lee, J. Lee, H. Yun, J. Kim, J. Park, C. Choi, D. C. Kim, H. Seo, H. Lee, J. W. Yu, W. B. Lee, D.-H. Kim, *Adv. Mater.* **2017**, *29*, 1702902.

[16] a) S. Chen, X. Zhang, J. Zhao, Y. Zhang, G. Kong, Q. Li, N. Li, Y. Yu, N. Xu, J. Zhang, K. Liu, Q. Zhao, J. Cao, J. Feng, X. Li, J. Qi, D. Yu, J. Li, P. Gao, *Nat. Commun.* **2018**, *9*, 4807; b) B. Conings, J. Drijkoningen, N. Gauquelin, A. Babayigit, J. D'Haen, L. D'Olieslaeger, A. Ethirajan, J. Verbeeck, J. Manca, E. Mosconi, F. D. Angelis, H.-G. Boyen, *Adv. Energy Mater.* **2015**, *5*, 1500477.

[17] a) B. Li, R. Long, Y. Xia, Q. Mi, *Angew. Chem., Int. Ed.* **2018**, *57*, 13154; b) C. Bao, J. Yang, S. Bai, W. Xu, Z. Yan, Q. Xu, J. Liu, W. Zhang, F. Gao, *Adv. Mater.* **2018**, *30*, 1803422; c) K. C. Tang, P. You, F. Yan, *Sol. RRL* **2018**, *2*, 1800075; d) M. Shoaib, X. Zhang, X. Wang, H. Zhou, T. Xu, X. Wang, X. Hu, H. Liu, X. Fan, W. Zheng, T. Yang, S. Yang, Q. Zhang, X. Zhu, L. Sun, A. Pan, *J. Am. Chem. Soc.* **2017**, *139*, 15592.

[18] a) Y. Liu, F. Li, L. Qiu, K. Yang, Q. Li, X. Zheng, H. Hu, T. Guo, C. Wu, T. W. Kim, *ACS Nano* **2019**, *13*, 2042; b) B. Jeong, H. Han, H. H. Kim, W. K. Choi, Y. J. Park, C. Park, *ACS Nano* **2020**, *14*, 1645.

[19] H. Zhang, Y. Liu, C. Yang, L. Xiang, Y. Hu, L. M. Peng, *Adv. Mater.* **2018**, *30*, 1805408.

[20] X. Li, D. Bi, C. Yi, J. D. Decoppet, J. Luo, S. M. Zakeeruddin, A. Hagfeldt, M. Gratzel, *Science* **2016**, *353*, 58.

[21] a) M. Zhang, Z. Zheng, Q. Fu, Z. Chen, J. He, S. Zhang, L. Yan, Y. Hu, W. Luo, *CrystEngComm* **2017**, *19*, 6797; b) S. W. Eaton, M. Lai, N. A. Gibson, A. B. Wong, L. Dou, J. Ma, L. W. Wang, S. R. Leone, P. Yang, *Proc. Natl. Acad. Sci. U S A.* **2016**, *113*, 1993.

[22] a) R. Nasanen, H. Ojanpaa, T. Tanskanen, J. Paallysaho, *Exp. Brain Res.* **2006**, *172*, 464; b) K. Rayner, T. J. Smith, G. L. Malcolm, J. M. Henderson, *Psychol. Sci.* **2009**, *20*, 6.

[23] Y. Tang, F. Wu, F. Chen, Y. Zhou, P. Wang, M. Long, W. Zhou, Z. Ning, J. He, F. Gong, Z. Zhu, S. Qin, W. Hu, *Small* **2018**, *14*, 1803158.